

Adjoint Slip Inversion under a Constrained Optimization Framework: Revisiting the 2006 Guerrero Slow Slip Event

J. Tago^{1,*}, V.M. Cruz-Atienza², C. Villafuerte², T. Nishimura³, V. Kostoglodov², J. Real² and Y. Ito³

1. Facultad de Ingeniería, Universidad Nacional Autónoma de México

2. Instituto de Geofísica, Universidad Nacional Autónoma de México

3. Disaster Prevention Research Institute, Kyoto University

June 26, 2020

Keywords: Slow slip inversion, Adjoint method, Guerrero Gap

Abstract

Understanding the faults behavior through geodetic data has an important impact in our assessment of the seismic hazard. To shed light on the aseismic evolution of geologic faults, we developed a new slip inversion strategy, the ELADIN (ELastostatic ADjoint INversion) method, that uses the adjoint elastostatic equations to efficiently compute the gradient of the cost function. To handle slip constraints, ELADIN is a 2-steps inversion algorithm. In the first step, it finds the slip that better explain the data without any slip constraints, and the second step refines the solution by imposing those constraints through a Gradient Projection Method. In order to get a physical plausible slip distribution and to overcome the poor fault illumination due to scarce data, ELADIN reduces the solution space by means of a von Karman autocorrelation function that controls the wavenumber content of the solution. Furthermore, to account for the data uncertainty, the method weights the observations depending on their covariance by means of the precision matrix. For estimating the resolution, we introduce a mobile checkerboard analysis that allows to determine lower-bound resolution zones over the fault for an expected slip-patch size and a specific stations array. We systematically test ELADIN with synthetic examples and use it to invert the 2006 Guerrero Slow Slip Event (SSE), which is one of the most studied SSEs in Mexico. Since only 12 GPS stations recorded the event, careful regularization is thus required to achieve reliable solutions. We compared our preferred slip solution with two previously published models and found that our solution preserves the most reliable characteristics of both models. Besides, although the three SSE models predict an updip penetration of the event into the seismogenic zone of the Guerrero seismic gap, our resolution analysis indicates that this penetration might not be a reliable feature of the 2006 event

*Corresponding author: Facultad de Ingeniería, Circuito Interior S/N, Mexico City, Zip Code 04510, phone: (+52)5556220850, email: josue.tago@gmail.com

27 Introduction

28 An elegant and powerful mean to solve geophysical inverse problems is the adjoint method (*AM*). Given an objective function,
29 \mathcal{C} , measuring the difference between data and a model prediction (i.e. a forward problem), to determine the model parameters
30 that minimize \mathcal{C} , the *AM* allows computing efficiently the derivative of \mathcal{C} with respect to the parameters by combining the
31 forward problem and the solution of an adjoint equation (i.e. of an adjoint problem) (Fichtner et al., 2006; Tromp et al., 2005;
32 Tarantola, 1984; Gauthier et al., 1986). Thus, the inverse problem can be solved by using any optimization method that exploits
33 that derivative to find the minimum of \mathcal{C} . The most important advantage of the *AM* is its efficiency to compute the derivative
34 of \mathcal{C} that, in many 3D geophysical inverse problems, is simply unaffordable. The *AM* has been successfully used to solve
35 full-waveform inverse problems in seismology, either to determine the elastic properties of the earth (Tromp et al., 2005; Askan
36 et al., 2007; Fichtner et al., 2010; Krischer et al., 2018) or the kinematic history of earthquake sources (Sánchez-Reyes et al.,
37 2018; Somala et al., 2018). However, to our knowledge no adjoint formulation has been proposed to invert geodetic data.

38 The slow secular displacement observed in the Earth's crust may be often explained in terms of the aseismic slip occurring
39 at the contact of tectonic plates. Depending on whether the interplate slip rate is larger than the relative plate motion, the
40 plate interface experiences either a coupling regime (i.e. creeping or full locking) (Simpson et al., 1988) or a slow slip event
41 (SSE) (Dragert et al., 2001). In the first case, the associated deformation could be explained through the backslip formulation
42 (Savage, 1983). In the second, a dislocation may predict the displacement field. In the real Earth, the surface displacement is
43 the summation of all contributions from the interface segments experiencing either a coupling regime or a SSE. In the case of
44 intra- or inter-plate active faults where aseismic slip or an earthquake may occur, the same approach holds true although an
45 earthquake will produce an instantaneous dislocation followed by a postseismic slow slip relaxation (Ozawa et al., 2011). In the
46 present work, to determine the plate interface aseismic slip history in these terms from continuous GPS (or any other geodetic)
47 measurements, we introduce and solve a constrained optimization problem based on the adjoint elastostatic equations with
48 Tikhonov regularization terms (Calvetti et al., 2000; Asnaashari et al., 2013) and a von Karman autocorrelation function (Mai
49 and Beroza, 2002; Amey et al., 2018). The new method, called ELADIN (ELastostatic ADjoint INversion), simultaneously
50 determines the distribution of the interplate coupling and slow slip from surface displacements.

51 In those cases where the crustal strain field corresponds to a quasi-static seismotectonic process, the surface displacement is
52 linearly related to the fault slip. However, determining the slip over an extended buried fault from such displacement remains an
53 ill-posed problem. Underdetermination of the model parameters (i.e. of the slip distribution) arises from the sparse sampling of
54 the displacement field and the rapidly decreasing sensitivity of displacement to slip with distance to the fault (Nocquet, 2018).
55 One rigorous framework to overcome this problem and to determine the uncertainty of such an inverse problem solution are the
56 Bayesian approaches. The incorporation of prior information through probability density functions (pdf) allows determining
57 the posterior model covariance and pdfs, as well as imposing model restrictions by means of truncated prior pdfs (Tarantola
58 and Valette, 1982; Nocquet, 2018; Minson et al., 2013; Yabuki and Matsu'Ura, 1992; Amey et al., 2018; Nocquet et al., 2014;

59 Nishimura et al., 2004). Although Bayesian approaches are widely used and powerful, one important limitation that most have
60 is the large computational load required to determine stochastically the posterior pdfs and thus the uncertainty of the model
61 parameters.

62 An alternative to solve the elastostatic inverse problem is by introducing model regularizations and physically consistent restric-
63 tions. To prevent unrealistic oscillatory slip distributions the most common regularization approach is to smooth the solution by
64 applying a Laplacian operator (i.e., penalizing the second derivative of the slip) (McCaffrey et al., 2007; Wallace and Beavan,
65 2010; Radiguet et al., 2011). Usually, the hyperparameter that controls the strength of the smoothing is chosen subjectively by
66 finding a satisfactory weight between the data fit and the smoothing of the slip distribution. One common strategy to determine
67 the hyperparameter is through an L-curve analysis that looks for an optimal hyperparameter value that keeps the data fitted
68 with the strongest possible regularization (Radiguet et al., 2011). From an statistical approach, the hyperparameter can be
69 determined using objective methods such as the Akaike's Bayesian Information criterion (ABIC) (Yabuki and Matsu'Ura, 1992;
70 Miyazaki et al., 2006) or fully Bayesian techniques (Fukuda and Johnson, 2008). Although the Laplacian operator reduces
71 unphysical and rough slip solutions (and thus unreliable large stress drops), this is not the most convenient mathematical strat-
72 egy to preserve the real nature of the slip when regularizing the problem, where the self-similarity of the fault slip observed in
73 earthquakes should be resolved as proposed by Amey et al. (2018).

74 When designing ELADIN, our goal was introducing a regularization approach that preserves the nature of faulting (i.e. the slip
75 self-similarity) and, at the same time, that allows a spectral control of the problem solution that guaranties a given resolution
76 criterion. To this purpose we introduce a von Karman autocorrelation function that reduces the solution space to a domain
77 where the wavenumber content of all possible solutions satisfies a minimum slip characteristic length previously determined
78 through robust resolution tests. We illustrate the capabilities of the method by inverting GPS data for the 2006 Guerrero SSE,
79 which has been widely investigated in the literature, and describe several benefits that our solution has as compared with some
80 previous models. Systematic inversion of GPS data along the entire Mexican subduction zone applying the ELADIN method is
81 presented in an associated work (Cruz-Atienza et al., 2020) where we analyzed the aseismic slip history of the plate interface
82 between 2017 and 2019.

83 **The ELADIN Method**

84 In this section, we first introduce the forward model that allows us to compute the synthetic displacements produced by a slip
85 over the fault. Then, we formulate the inverse problem in a constrained optimization framework, reducing the solution space
86 to control its spectral content with a von Karman correlation function. We also include a Tikhonov term to penalize regions
87 where slip is not expected to occur and to impose slip magnitude constraints. Finally, we present a 2-step algorithm that first
88 solves the inverse problem without slip constraints using the adjoint equations for the gradient computation. Then we project

89 the resulting solution into the feasible solution space to initiate the second step by following the Gradient Projection method to
 90 optimize the solution by respecting the desired slip constraints.

91 Forward model

92 The elastostatic representation theorem for the displacement field, $\underline{u}(\underline{x})$, due to a slip, $\underline{d}(\underline{\xi})$, produced at a fault, Σ , is

$$u_j(\underline{x}) = \int_{\Sigma} T_k(S_{ij}(\underline{\xi}, \underline{x}), \hat{n}(\underline{\xi})) d_k(\underline{\xi}) d\Sigma, \quad i, j, k \in \{x, y, z\}, \quad (1)$$

93 where $T_i(\cdot, \cdot)$ is the i -component of the traction vector on the fault computed through the Somigliana tensor, $S_{ij}(\underline{\xi}, \underline{x})$, and
 94 the fault normal vector $\hat{n}(\underline{\xi})$. If the traction and the slip are projected along the plate convergence direction, c -, and the
 95 complementary perpendicular direction, p -direction, eq. (1) can be written in matrix form as

$$\begin{aligned} \begin{bmatrix} u_1(\underline{x}) \\ u_2(\underline{x}) \\ u_3(\underline{x}) \end{bmatrix} &= \int_{\Sigma} \begin{bmatrix} T_p(S_{i1}(\underline{\xi}, \underline{x}), \hat{n}(\underline{\xi})) & T_c(S_{i1}(\underline{\xi}, \underline{x}), \hat{n}(\underline{\xi})) \\ T_p(S_{i2}(\underline{\xi}, \underline{x}), \hat{n}(\underline{\xi})) & T_c(S_{i2}(\underline{\xi}, \underline{x}), \hat{n}(\underline{\xi})) \\ T_p(S_{i3}(\underline{\xi}, \underline{x}), \hat{n}(\underline{\xi})) & T_c(S_{i3}(\underline{\xi}, \underline{x}), \hat{n}(\underline{\xi})) \end{bmatrix} \begin{bmatrix} d_p(\underline{\xi}) \\ d_c(\underline{\xi}) \end{bmatrix} d\Sigma, \quad i \in \{x, y, z\} \\ \underline{u}(\underline{x}) &= \int_{\Sigma} \underline{T}(\underline{\xi}; \underline{x}) d(\underline{\xi}) d\Sigma. \end{aligned} \quad (2)$$

96 Then, the fault is discretized in M subfaults such that the integral can be approximated as

$$\underline{u}(\underline{x}) \simeq \sum_{i=1}^{M \text{ subfaults}} A^i \underline{T}(\underline{\xi}^i; \underline{x}) d(\underline{\xi}^i), \quad (3)$$

97 where A^i is the i -subfault area. Finally, if we want to compute the displacement for N receivers, we can order the displacements
 98 in a single vector such that the entire computation is reduced to a simple matrix-vector product as

$$\begin{aligned} \begin{bmatrix} \underline{u}(\underline{x}^1) \\ \underline{u}(\underline{x}^2) \\ \vdots \\ \underline{u}(\underline{x}^N) \end{bmatrix} &= \begin{bmatrix} A^1 \underline{T}(\underline{\xi}^1; \underline{x}^1) & A^2 \underline{T}(\underline{\xi}^2; \underline{x}^1) & \cdots & A^M \underline{T}(\underline{\xi}^M; \underline{x}^1) \\ A^1 \underline{T}(\underline{\xi}^1; \underline{x}^2) & A^2 \underline{T}(\underline{\xi}^2; \underline{x}^2) & \cdots & A^M \underline{T}(\underline{\xi}^M; \underline{x}^2) \\ \vdots & \vdots & \ddots & \vdots \\ A^1 \underline{T}(\underline{\xi}^1; \underline{x}^N) & A^2 \underline{T}(\underline{\xi}^2; \underline{x}^N) & \cdots & A^M \underline{T}(\underline{\xi}^M; \underline{x}^N) \end{bmatrix} \begin{bmatrix} \underline{d}(\underline{\xi}^1) \\ \underline{d}(\underline{\xi}^2) \\ \vdots \\ \underline{d}(\underline{\xi}^M) \end{bmatrix}, \\ \underline{U} &= \underline{T} \underline{D}, \end{aligned} \quad (4)$$

99 where $\underline{U} \in \mathbb{R}^{3N}$, $\underline{T} \in \mathbb{R}^{3N \cdot 2M}$ and $\underline{D} \in \mathbb{R}^{2M}$.

100 Inverse problem

101 The inverse problem consists in recover the slip at each subfault of a known interface that produces displacements observed
 102 at geodetic stations. Due to the linearity of the forward model, eq. (4), we construct a quadratic cost function to formulate a
 103 convex inverse problem as

$$\mathbb{C}(\underline{D}) = \frac{1}{2} [\underline{U} - \underline{U}_o]^T [\underline{U} - \underline{U}_o], \quad \text{s.t.} \quad \underline{U} = \underline{T}\underline{D}, \quad (5)$$

104 where $\underline{U}_o \in \mathbb{R}^{3N}$ are the displacements observed at the N geodetic stations stored in a single ordered vector, as we did with \underline{U}
 105 in eq. (4). Since real data are sparse and may have significant noise, the inverse problem (5) is ill-conditioned. In order to face
 106 these issues, a problem regularization and realistic physical constraints are introduced next.

107 Problem Regularization: von Karman autocorrelation function

108 Most often, the problem regularization is done by means of two elements: a model precision matrix and/or Tikhonov terms.
 109 The model precision matrix is the inverse of the model covariance matrix which, in our case, controls how sensitive is the slip
 110 in a given subfault to the slip on its neighbor subfaults. Radiguet et al. (2011) proposed a subfault correlation that follows a
 111 decreasing exponential function according to a defined correlation length. The problem we found with this approach is that
 112 the precision matrix for different correlation lengths does not have significantly different effects due to the fast decay of that
 113 function. For different types of correlation functions we tested, the model covariance matrix starts to become ill conditioned
 114 when the subfaults size becomes smaller than the correlation length.

115 Tikhonov terms added to the cost function are used to penalize the roughness of the solution. Generally, the penalization
 116 is applied to the first or second spatial derivatives of the slip. Exercised we performed revealed that, when penalizing the
 117 derivatives, the norm of the slip solution is usually reduced as well. Besides, these two alternatives involve hyperparameters
 118 that need to be optimally determined because they control de tradeoff between the misfit of the data and the strength of the
 119 regularization.

120 These inconveniences lead us to propose a new approach that reduces the solution space so that the wavenumber content of
 121 the solution (i.e. the minimum characteristic length of the slip patches) can be controlled. The main idea is to apply a filter
 122 operator, \underline{E} , to the slip \underline{D} . Then, the cost function (5) can be formulated as

$$\mathbb{C}(\underline{D}) = \frac{1}{2} [\underline{U} - \underline{U}_o]^T \underline{C}_d^{-1} [\underline{U} - \underline{U}_o], \quad \text{s.t.} \quad \underline{U} = \underline{T}\underline{E}\underline{D}, \quad (6)$$

123 where \underline{C}_d is the data covariance matrix that we introduce to weight the data according to their quality or importance.

124 Recently, Amey et al. (2018) showed that a von Karman regularization for slip inversions is a good strategy to guarantee the

125 slip self-similar properties (Mai and Beroza, 2002) that can not be achieved with a common Laplace regularization. The spatial
126 von Karman autocorrelation function is

$$vk(r) = \frac{r^H K_H(r)}{(1e^{-10})^H K_H(1e^{-10})}, \quad (7)$$

127 where H is the Hurst exponent, $K_H(\cdot)$ is the modified Bessel function of second kind of order H , r is the correlation length
128 that can be computed as

$$r = \sqrt{\frac{s^2}{a_s^2} + \frac{d^2}{a_d^2}}, \quad (8)$$

129 where (s, d) are the coordinates in the along-strike and along-dip directions on the fault, and (a_s, a_d) are the correlation lengths
130 in the same directions. This autocorrelation function can be used to construct a linear operator K which, convolved with the
131 slip D , controls the wavenumber content of the output function along both the strike and dip component. This convolution can
132 be formulated as a matrix-vector product where the matrix operator, \underline{F} , applies the convolution of the linear operator K to the
133 slip, \underline{D} , as was done in eq. (6).

134 Slip constraints

135 The model regularization we introduced guarantees that an optimal slip solution can be found. However, this solution may
136 violate some expected physically-consistent restrictions such as the full-coupling regime limit or slip rakes consistent with the
137 plate convergence direction. Thus, slip constraints need to be imposed according to the available information. The cost function
138 (6) can then be reformulated as

$$\mathbb{C}(\underline{D}) = \frac{1}{2} [\underline{U} - \underline{U}_o]^T \underline{C}_d^{-1} [\underline{U} - \underline{U}_o] + \frac{\beta}{2} [\underline{W}(\underline{F}\underline{D} - \underline{D}_p)]^T [\underline{W}(\underline{F}\underline{D} - \underline{D}_p)], \quad (9)$$

s.t.

$$\underline{U} = \underline{T}\underline{F}\underline{D}, \quad (10)$$

$$D_i^{j,l} \leq (\underline{F}\underline{D})_i \leq D_i^{j,u}, \quad i \in \{p, c\} \wedge j \in \{\text{SSE}, \text{Coupling}\} \text{ regime}, \quad (11)$$

139 where β is a hyperparameter, \underline{W} is a model-weight diagonal matrix that penalizes the slip per subfaults, \underline{D}_p is an *a priori* slip
140 solution and $(D_i^{j,l}, D_i^{j,u})$ are the lower and upper limits of the i -component of the slip in the j -regime. The slip is either in
141 the SSE regime if its c -component is opposite to the plate convergence direction or in the coupling regime otherwise. If we
142 have an *a priori* slip solution, \underline{D}_p , we can force the solution to be as close as possible to it by accepting only model changes
143 that improve the data fit. In that case, the weight matrix should be the identity matrix, $\underline{W} = \underline{I}$. If no *a priori* slip information
144 is available, we simply set $\underline{D}_p = 0$ and, to obtain the minimum norm solution, we make again $\underline{W} = \underline{I}$. Since we are not
145 interested in getting the minimum norm solution in the present study, we thus set $\underline{W} = 0$ everywhere except in the subfaults
146 where we assume free slip (i.e. no coupling or SSE regime). The bigger the weighting value, the bigger is the subfaults slip
147 penalization. The hyperparameter β controls the tradeoff between the fit of the data and the slip constraints imposed in the cost

148 function. However, since it is in the slip penalization term, its value should only guarantee that the solution does not contain
 149 significant slip in the penalized regions. On the other hand, if an *a priori* slip solution ($\underline{D}_p \neq 0, \underline{W} = \underline{I}$) is used or a minimal
 150 norm solution ($\underline{D}_p \neq 0, \underline{W} = \underline{I}$) is desired, then β must be determined following an optimal strategy as an L-curve analysis
 151 (e.g. Radiguet et al. (2011)) or the ABIC criterion (e.g. Miyazaki et al. (2006)).

152 Gradient computation: Adjoint method

153 To solve the inequality-constrained inverse problem (eqs. (9), (10) and (11)), first we address the gradient of the cost function
 154 without considering the inequality constraints, eq. (11). In the framework of constrained inverse problems, the Lagrangian can
 155 be computed as

$$\mathcal{L}(\underline{D}, \underline{U}, \underline{\lambda}) = \mathbb{C}(\underline{D}) + \underline{\lambda}^T \left[\underline{U} - \underline{\mathcal{T}}\underline{F}\underline{D} \right], \quad (12)$$

156 where $\underline{\lambda}$ are the Lagrange multipliers. The Lagrangian total derivative with respect to the slip, \underline{D} , is

$$D_{\underline{D}}\mathcal{L} = \nabla_{\underline{D}}\mathcal{L} + \nabla_{\underline{U}}\mathcal{L} \cdot \nabla_{\underline{D}}\underline{U} + \nabla_{\underline{\lambda}}\mathcal{L} \cdot \nabla_{\underline{D}}\underline{\lambda}. \quad (13)$$

157 To simplify the computation of the gradient, we follow the adjoint method strategy (Fichtner et al., 2006). We start forcing
 158 $\nabla_{\underline{\lambda}}\mathcal{L} = 0$ by solving a forward model $\tilde{\underline{U}} = \underline{\mathcal{T}}\underline{F}\underline{D}$. Then, we use the predicted displacement, $\tilde{\underline{U}}$, to compute the adjoint source
 159 as $\tilde{\underline{\lambda}} = \underline{C}_d^{-1} \left[\underline{U}_o - \tilde{\underline{U}} \right]$ which implies $\nabla_{\underline{U}}\mathcal{L} = 0$. As a result, the Lagrangian total derivative is the solution of the adjoint
 160 problem plus a term related with the slip constraints as

$$\begin{aligned} D_{\underline{D}}\mathcal{L} &= \nabla_{\underline{D}}\mathcal{L} \\ &= -(\underline{\mathcal{T}}\underline{F})^T \tilde{\underline{\lambda}} + \beta \left[\underline{F}^T \underline{W}^T \underline{W} \left(\underline{F}\underline{D} - \underline{D}_p \right) \right]. \end{aligned} \quad (14)$$

161 Once the gradient of the cost function has been evaluated, we can follow any numerical optimization strategy to find the set of
 162 model parameters that minimize that function.

163 Gradient Projection Method

164 To avoid dealing with inequality constraints, it is often convenient to project the solution into the physically-consistent space
 165 after each iteration of the inversion procedure. However, for the slip inversion we realized that such projection is not convenient
 166 because, frequently, the gradient direction is orthogonal to the slip constraints making the algorithm to stop. For large scale
 167 problems with lower and upper bounds for the variables, Nocedal and Wright (2006) propose the Gradient Projection Method
 168 (GPM) as an efficient strategy to deal with inequality restrictions. The GPM consists of two stages per iteration. In the first
 169 stage, the steepest descent direction is followed until a bound, i.e. the limit of an inequality constraint, is encountered which
 170 needs to be bent to stay feasible. Then along the resulting piecewise-linear path, a local minimizer, called *Cauchy point*, is

171 found (see Appendix A for details). For the second stage, a new optimum point is searched in the face of the feasible box on
172 which the Cauchy point lies, i.e. those slip constraints that have reached a limit are changed to equality constraints. It implies
173 that those inequality constraints now are part of the active set. This subproblem is usually not solved exactly since the remaining
174 inequality constraints are usually not considered.

175 For the slip inversion, we do not follow exactly the GPM to avoid the subproblem of the second stage. Mainly because we
176 expect that many subfaults in the coupling regime achieve its slip limit and that the number of iterations required was difficult
177 to define. So, after computing the Cauchy point, we directly take it as a new iteration point where the gradient is computed
178 again. Thus, it is essentially a steepest descent algorithm that respects the inequality constraints. Our GPM version is slow so
179 to achieve a fast convergence, we then propose an algorithm that is explained in the next section.

180 **2-step inversion algorithm**

181 In order to increase the convergence speed, we developed a 2-step inversion algorithm. The purpose of the first step is to get
182 an optimal initial solution for the GPM. In this step, we solve the unconstrained slip inverse problem using the adjoint method
183 to compute the gradient of the cost function. Once the gradient is obtained, any iterative optimization algorithm can be used to
184 find the optimal solution, e.g. the Conjugate Gradient method, the l-BFGS method, etc. In this work, we use the SEISCOPE
185 optimization toolbox, which is a friendly and powerful optimization library developed in FORTRAN 90 with many available
186 optimization strategies (Métivier and Brossier, 2016). After some performance trials, we decided to use the l-BFGS method. In
187 the second step, we first project the solution into the physically-consistent domain and then we solve the constrained slip inverse
188 problem with a slight modification of the GPM. As explained above, after computing the Cauchy point, instead of reformulating
189 the inverse problem according to the new active set incorporating some inequality constraints, we use it as the new iteration of
190 the slip. This is not a fast strategy, but since we start from a slip distribution that is close to the optimal solution, only a few
191 iterations of the GMP are required (about 200). The pseudocode is described in Algorithm 1.

Algorithm 1: 2-Steps Algorithm**1st Step:** Unconstrained slip inverse problem (Adjoint method)**Data:** GPS DataInitialize the slip $\underline{D}_0 = 0$;**while** Convergence is not achieved **do**

1. Compute a forward problem

$$\underline{U}_k = \underline{T}\underline{E}\underline{D}_k.$$

2. Compute the adjoint source

$$\underline{\lambda}_k = \underline{C}_d^{-1} [\underline{U}_o - \underline{U}_k].$$

3. Compute the adjoint problem to get the gradient

$$\nabla_{\underline{D}} \mathcal{L} = -(\underline{T}\underline{E})^T \underline{\lambda}_k + \beta \left[\underline{E}^T \underline{W}^T \underline{W} (\underline{E}\underline{D}_k - \underline{D}_p) \right]$$

4. With the gradient use any iterative optimization algorithm to find an update step $\Delta \underline{D}_k$

5. Update the slip

$$\underline{D}_{k+1} = \underline{D}_k + \Delta \underline{D}_k.$$

end**2nd Step:** Constrained slip inverse problem (Gradient Projection Method)**Data:** Optimal solution of 1st step, \underline{D}^* Project \underline{D}^* into the physically-consistent domain to get the initial solution \underline{D}_0 ;**while** Convergence is not achieved **do**1. From \underline{D}_k compute the Cauchy point \underline{D}_k^c (details in Appendix A)

2. Update the slip

$$\underline{D}_{k+1} = \underline{D}_k^c.$$

end**Resolution**

Resolution of our inverse problem essentially depends on the geometry configuration of the problem. This is, on the fault geometry and the distribution of observation sites (i.e. on the displacement field sampling and the sensitivity of displacement to dislocations in the fault). For a given problem discretization, synthetic inversions are a powerful mean to quantify how well an inverse method performs. If well-conceived, these tests may lead to very useful resolution information under realistic conditions (i.e. if they include data uncertainties and minimize the dependence on the target model). In the following, we

199 present comprehensive exercises where the restitution of the target model is systematically quantified. To this purpose, for a
 200 given slip solution we define the restitution index, r_i as

$$r_i = 1 - \left| \frac{d_i^T - d_i^I}{d_i^T} \right|, \quad (15)$$

201 where d_i^T and d_i^I are the slip or the target and inverted models at the i -subfault, respectively. The slip component used to
 202 determine the restitution index can be either the plate convergence or its perpendicular direction. We also introduce the average
 203 restitution index, ari , which is the mean of the restitution indexes over the M subfaults that discretize the 3D subduction
 204 interface between the Cocos and the North American plates in central Mexico (Cruz-Atienza et al., 2020). r_i is one if the
 205 inverted slip equals the target slip and zero if the difference between them equals the target value. We have discretized the
 206 plate interface with subfaults whose surface projection is a square of $10 \times 10 \text{ km}^2$. To compute the static traction vectors along
 207 the interface due to single body forces at the stations, eq. (1), we assumed a four-layer 1D structure suitable for the region
 208 (Campillo et al., 1996) and used the AXITRA method (Coutant, 1990). For the analysis, we have considered all available
 209 permanent GPS stations (66 sites) in central Mexico (Cruz-Atienza et al., 2020) and 5 ocean bottom pressure gauges (OBP)
 210 deployed in the Guerrero seismic gap since November 2017 (Cruz-Atienza et al., 2018), where only the vertical displacements
 211 were considered.

212 **Mobile checkerboard**

213 A widely used strategy to quantify an inverse problem resolution is the checkerboard (CB) test. However, this test is intrinsically
 214 linked to the arbitrary choice of the target CB model, which means to the CB unit size, its positions and the absolute model-
 215 properties periodically attributed. For this reason, we performed comprehensive mobile checkerboard (MOC) tests for different
 216 patch sizes (PS). Based on previous GPS data inversions in central Mexico (Radiguet et al., 2012; Cruz-Atienza et al., 2020),
 217 we attributed patch slip values in the plate convergence direction of 30 cm (i.e. as typical SSEs in the region) and -10 cm (i.e.
 218 a backslip corresponding to 20 months of full coupling assuming a 6 cm/y plate convergence rate).

219 Figure 1 shows the inversion results for three CBs with different PS (i.e. 60, 80 and 100 km) and the same correlation length
 220 (i.e. $L = 20 \text{ km}$). As we shall see, this value of L maximizes the average restitution index (ari) in these cases where no
 221 slip restrictions were imposed (i.e. no gradient projection method was used) and no data uncertainty was considered (i.e. the
 222 precision matrix was the identity matrix). Although the data fit is almost perfect in all three cases, it is clear that the target
 223 model restitution strongly depends on PS, the slip model characteristic length. As expected, the larger PS the better is the
 224 restitution. This is quantified in the right column, where the restitution index, r , is displayed for all subfaults. Besides, two
 225 more conclusions stand out: (1) restitution is better in SSE patches than in coupling patches, and (2) the inversion scheme
 226 cannot resolve the unrealistic slip discontinuity along the boundary of the CB patches. Both conclusions were expected because
 227 the backslip is one third of the positive slip, and because of both the imposed model regularization and the limited sensitivity

228 of displacements with distance to the fault.

229 Previous results do not provide a reliable estimate of the problem resolution when facing real data because in that case we do not
 230 know the actual slip producing the observed displacements. A MOC test consists in multiple CB inversions so that all possible
 231 model positions are explored. Results from the test may be translated into the mobile checkerboard restitution index (*mcri*) per
 232 subfault, which corresponds to the average of the *r* values estimated for each inversion. The *mcri* is a quantity that eliminates
 233 the resolution dependence on the CB position. For a given PS, we performed 6 MOC tests, one without regularization (i.e. L
 234 $= 0$ km) and the rest with different correlation lengths (i.e. for $L = 10, 20, 30, 40$ and 50 km). Five different PS of $40, 60, 80,$
 235 100 and 120 km were considered so each case required a different number of CB inversions to complete the associated MOC
 236 test. Since the horizontal projection of the subfaults is 10 km per side and we shifted the CBs with a 20 km jump along the dip
 237 and strike directions to complete all possible configurations, the total number of CB inversions in a MOC test for an given PS
 238 is $(PS/10)^2$.

239 Figure 2 presents an overview of three MOC tests for PS of $60, 80$ and 100 km (i.e. those considered in Figure 1). As expected,
 240 in the top row, we see that the *mcri* increases with the PS, reaching values close to 0.8 in some regions close to the coast where
 241 there is the largest density of stations, and where the plate interface is closest to them. In deeper interface regions, between 30
 242 and 50 km depth, *mcri* falls down up to about 0.2 for PS of 60 km and over 0.5 for PS of 100 km along the whole subductions
 243 zone. As clearly seen in the right column of Figure 1, the unrealistic slip discontinuities along the patches edges strongly
 244 difficults the restitution, so we can considerer the *mcri* maps of Figure 2 (first row) as a lower resolution bound. Isocontours
 245 of these maps for different PSs and optimum correlation lengths thus define reliable fault regions where the inversions should
 246 resolve the unknown target slip above the *mcri* isocontour value (e.g., above 40% of the target slip if *mcri* equals 0.4).

247 The MOC tests also allow to identify the optimum correlation length per subfault that maximizes the *ari*. This is shown in
 248 the second row of Figure 2, where we see that L decreases for PS of 100 km along the coast as compared with smaller slip
 249 characteristic lengths (i.e. for smaller PSs). The opposite happens in deep and less instrumented interface regions, where L
 250 increases with PS. Notice also that regularization should be stronger offshore, close to the subduction trench, as PS decreases.
 251 Based on this multiscale analysis we assembled optimum solutions for the same CBs of Figure 1 by integrating the best inverted
 252 slip per subfault (i.e. for the optimum local regularization). Resolution improvements for the multiscale models ranged between
 253 10% and 20% as shown in the third row of the figure (compare with the right column of Figure 1). However, something
 254 unexpected came out when comparing whole-interface average *mcri* values for all MOC tests. Figure 3 shows this metric
 255 along with the average data-misfit error (i.e. the L_2 norm of the difference between target and inverted displacements) for all
 256 tested PSs as a function of L , the correlation length. Although the spatial distribution of the optimum L depends on the slip
 257 characteristic length PS, the best average regularization was the same for all PSs and equal to 20 km. Such independency of the
 258 average *mcri* on L for different PSs is strongly determined by the unrealistic slip jumps of the checkerboards slip values that

259 sweep the whole interface no matter the PS. However, as we shall see later, the optimal regularization length actually increases
260 with PS if both the data uncertainty (i.e. the precision matrix) and the slip restrictions (i.e. the GPM method) are considered in
261 the inversions. What is remarkable and was indeed expected in Figure 3 is that (1) the maximum restitution values increased
262 with PS, (2) the restitution function for a given PS displayed a concave behavior and (3) the best fitting models are not the best
263 solutions (i.e. those with the highest restitution). Regularization is thus critical to achieve physically acceptable and reliable
264 slip models.

265 **Gaussian slip**

266 The analysis of the previous section did not consider the uncertainty in geodetic measurements that may be significantly large,
267 especially in the vertical component where atmospheric noise and non-tectonic physical signals are particularly present. Nor did
268 the analysis incorporate slip restrictions that are essential to guarantee tectonic expectations in our slip solutions such as backslip
269 smaller than expected for a full-coupled interface regime and slip rake angles close to the plate convergence direction. For this
270 reason, we now study three synthetic exercises where (1) the target slip corresponds to truncated Gaussian slip distributions (i.e.
271 to an SSE) surrounded by a full-coupled plate interface, and (2) the associated surface displacements (i.e. the inverted data) are
272 strongly and randomly perturbed according to a normal probability distribution given by the data covariance per component,
273 which we took as 2.1, 2.5 and 5.1 mm in the north, east and vertical directions, respectively (Radiguet et al., 2011).

274 Figure 4 shows the target slip models and both, the associated exact displacements (blue arrows) and the perturbed ones (red
275 arrows). The data uncertainty is represented by the gray ellipses at the tips of the perturbed vectors, the semiaxes corresponding
276 to the standard deviation of the normal distribution used to perturb the data per component. The interplate coupling corresponds
277 to three-months cumulative backslip assuming a 6 cm/yr plate convergence (i.e. 1.5 cm), and the geometry and position of the
278 three Gaussian slip patches were inspired by recent SSE solutions found in the region (Cruz-Atienza et al., 2020). Please notice
279 how large are the perturbations.

280 Inversions for the three Gaussian slip models were done for both the exact and perturbed data. Each set of data was inverted
281 without regularization and with correlation lengths of 10, 20, 30, 40, 50 and 60 km. In all cases backslip restrictions were applied
282 by means of the GPM so the interplate coupling could never overcome the value of one. Figure 5A shows some slip solutions
283 for the largest-Gaussian exact data together with the associated restitution maps. Although the data fit is excellent in all cases,
284 acceptable solutions are only retrieved when model regularization is applied. For $L = 30$ km, the *ari* is above 0.9 so that the
285 slip solution is almost perfect, except along the Gaussian contour where there is an unrealistic slip discontinuity in the target
286 model (i.e. a similar problem as for the checkerboards of last section).

287 When random noise is added to the theoretical observations and the inverse problem is solved by integrating the data uncertainty
288 by means of the precision matrix, the model regularization becomes even more critical to achieve a reliable solution. This can

289 be seen in Figure 5B, where the restitution is very poor around the Gaussian slip area when no regularization is applied as
 290 compared with that for $L = 40$ km, where the *ari* is also above 0.9 and thus the slip solution is surprisingly good. Also
 291 astonishing, results for the other two, smaller Gaussian slip models were very similar (see Appendix B, Figures S1 and S2). A
 292 summary of the 42 inversions (i.e. 14 per Gaussian model) is shown in Figure 6, where we see that although the data-fitting
 293 errors for the noisy inversions are roughly four times larger than those obtained from the exact data, the *ari* in all cases is
 294 above 0.9 for the best solutions (i.e. for the optimum L) even for the smallest and circular Gaussian case, which has a slip
 295 characteristic length smaller than 80 km centered at 38 km depth (Figure 4A).

296 **The 2006 Guerrero SSE**

297 During 20 years preceding the devastating 2017 Mw8.2 Tehuantepec earthquake that took place offshore the Oaxaca state,
 298 Mexico, long term SSEs in Guerrero occurred almost every four years (i.e. six events between 1998 and 2017) and had a
 299 remarkably large moment magnitudes ($M_w > 7.5$) (Kostoglodov et al., 2003; Radiguet et al., 2012; CruzAtienza et al., 2018).
 300 After the earthquake, the regional plate-interface SSE beating has strongly changed so that two other SSEs took place in that
 301 state in the next two years (in 2018 and 2019) with much smaller magnitudes (M_w around 7.0) (Cruz-Atienza et al., 2020).
 302 Among all Mexican SSEs, the 2006 Guerrero event has been the most investigated despite the poor GPS instrumentation on
 303 that time (Kostoglodov et al., 2010; Vergnolle et al., 2010; Radiguet et al., 2011, 2012; Cavalié et al., 2013; Bekaert et al., 2015;
 304 Villafuerte and Cruz-Atienza, 2017). One of its most interesting features is that, unlike adjacent subduction segments, the slow
 305 slip seems to have penetrated the updip seismogenic region of the plate interface up to 15 km depth in the Guerrero seismic
 306 gap. In this section we perform a thorough analysis of the inverse problem resolution for that event and provide what we think
 307 are its most reliable features as compared with previous results reported in the literature.

308 **Resolution**

309 In previous sections we found that the problem resolution depends on two main parameters: (1) the slip characteristic length
 310 (PS) and (2) the inverse-problem correlation length (L). This is true for a given problem geometry (i.e. for a stations array and
 311 plate interface geometry). For this reason, we can determine fault regions where resolution (i.e. the restitution index) is high
 312 enough for a given L and PS, which means that the inverted slip in those regions is valid within the wavenumber bandwidth
 313 associated to the von Karman spectrum for that L . Since only 12 significant GPS stations registered the 2006 SSE, we performed
 314 three different MOC tests considering only the location of these sites and CP periodic pc-slip values of -8 and 25 cm. The tests
 315 were done for checkerboard unit lengths (PS) of 80, 100 and 120 km, and for $L = 0$ (no regularization), 10, 20, 30, 40, 50 and
 316 60 km. This resolution exercises assumed reasonable backslip and rake angle restrictions by means of the GPM (i.e. a lower
 317 slip limit of -8 cm, and a rake angle restriction of $[20, -20]^\circ$ range with respect to the pc-direction.

318 Plate-interface resolution maps (i.e. for the *mcri* metric) are shown in Figure 7 as a function of PS and L. As expected,
319 overall *mcri* values increase with PS for a given L. Although less evident, they also increase with L for a given PS. However,
320 supplementary results not shown reveal that, in the latter case, the high-resolution regions stop expanding for L above 30 km for
321 all three PS cases. The maps show isocontours for $mcri = 0.6$, which delineate fault regions where the slip solutions are likely
322 to resolve the actual slip within 40% error. As explained previously, these maps represent a lower resolution bound because the
323 MOC tests assume unrealistically sharp slip discontinuities that strongly penalize the restitution index due to the boundaries of
324 the square slip patches (e.g. see Figure 1). For this reason, we expect the resolution within the regions to be higher than the
325 *mcri* isocontours value. Either way, even in the MOC test for the maximum PS and L values, the high resolution region does
326 not extend across the whole expected SSE area, as claimed by previous authors using different inversion techniques (Radiguet
327 et al., 2011). Our resolutions maps represent the key piece allowing us to tell something reliable (to some point) about the 2006
328 SSE.

329 Figure 8 summaries the results from all MOC tests in terms of the average *mcri* and data-misfit L2 error. Although errors are
330 similar for all slip characteristic lengths PS, the maximum average *mcri* value increase with PS and follow a concave trajectory
331 with L as previously noticed from Figure 7. However, unlike the previous MOC exercises considering all currently available
332 geodetic stations (Figures 2 and 3), the optimum correlation lengths (i.e. those maximizing the restitution) increase with PS.
333 This remarkable and reasonable result is due to both the slip restrictions and the sparse stations array. It tells us that, depending
334 on the characteristic size of the SSE patch we want to solve best, the regularization of the problem must be adapted. For
335 instance, if we are interested in SSE patches with a characteristic length of 80 km, then $L = 10$ km is the optimum choice. Of
336 course, such small value is detrimental to the extent of the acceptable resolution region, as seen in Figure 7. If $L = 20$ km, then
337 patches with characteristic length of 100 km will be optimally solved in a larger fault region.

338 **2006 SSE Inversions**

339 The next inversions we present were done using the same GPS data as Radiguet et al. (2011). This means that the displacement
340 timeseries were carefully pre-processed (Vergnolle et al., 2010) and then corrected for inter-SSE long-term deformations by
341 subtracting the linear trends from the period 2003-2005 per station. The resulting time series thus show the deviations from the
342 long-term steady motion during the 2006 Guerrero SSE.

343 Since the inter-SSE displacement trends per station are significantly different in Guerrero (Radiguet et al., 2012), the data
344 correction makes the time series difficult to interpret altogether. By removing the secular deformation patterns, we are implicitly
345 eliminating the common reference frame given by the North American plate, which also leads to a possible overestimation of
346 the SSE-induced displacements. Either way, for the sake of comparison with previous solutions using this dataset, we have
347 inverted the time series from January 30 (2006) to January 15 (2007) for four different correlations lengths ($L = 10, 20, 30$
348 and 40 km) and considering slip restrictions (i.e. applying the GPM), so that the backslip could not overcome the full-coupling

349 regime in that period and the rake vector could vary $\pm 20^\circ$ from the plate-convergence (pc) direction.

350 Figure 9 shows the inversion results for two optimal correlation lengths ($L = 20$ and 30 km). Since the data is almost perfectly
 351 explained in both cases, the preferred solution will depend on both the scale at which we are interested in for interpretations and
 352 reasonable physical considerations. Taking the 1 cm slip contour as the effective SSE area, then the moment magnitude of the
 353 2006 event is consistent for both inversions and equal to $M_w 7.4$. For estimating M_w , we considered a typical crustal rigidity
 354 $\mu = 32 \times 10^9$ Pa.

355 As shown in the last section, given the poor GPS coverage during the 2006 SSE, the inverse problem regularization plays
 356 a critical role to have some confidence in the slip solutions. In the absence of resolution analysis, it is difficult to justify
 357 any conclusion, especially between distant stations. For instance, the absence of data along most of the north-west Guerrero
 358 seismic gap (NW-GGap) (i.e. between ZIHP and CAYA) (UNAM, 2015) and the Guerrero Costa Chica (i.e. between CPDP and
 359 PINO) is unfortunate and obliges us to be cautious in the interpretations. Previous investigations concluded that SSEs behave
 360 differently between these two Guerrero subduction segments so that, unlike the Costa Chica, the slow slip in the NW-GGap
 361 reaches the updip seismogenic interface zone (i.e. up to 15 km depth) (Radiguet et al., 2011; Cavalié et al., 2013) releasing
 362 aseismically a significant part of the accumulated inter-SSE strain (Radiguet et al., 2012; Bekaert et al., 2015).

363 Figure 10 shows a comparison between our preferred solution (model A) (i.e. for $L = 30$ km) and two previously published
 364 solutions, one from the simultaneous inversion of both GPS and InSAR data (Model B by Cavalié et al. (2013)) and the
 365 other from GPS data only (model C by Radiguet et al. (2011)). Our solution is shown together with the associated 60%
 366 resolution regions (regions where the average m_{cri} is higher than 0.6), which are taken from Figure 7 according to the optimal
 367 solutions of Figure 8. Confidence contours thus delineate the fault regions where solutions disagree with the actual slip by
 368 less than 40% in different wavenumber bandwidths depending on L . The red contour delineate the 60% confidence regions
 369 for a slip characteristic length of 80 km, while the green contours depict the same regions for a 120 km characteristic length.
 370 Although the three slip solutions are in general consistent, there are clear differences among them. The most visible are (1) the
 371 concentration of separated patches in model C (i.e. one of them far from the coast and below 40 km depth, and another one
 372 to the east) which may be artifacts to explain the data due to a lack of regularization as neither of both are present in solutions
 373 A and B, which are consistent north of the CAYA and COYU stations, and (2) the peak slip values that range between 20 and
 374 25 cm. Moment magnitudes are also slightly different (i.e. 7.4 and 7.6 for models A and C, respectively). However, all three
 375 models coincide on the updip SSE spreading west of station CAYA, where our model has resolution higher than 60% up to a
 376 distance no more than 30 km west of that station. This region is of critical importance because it extends along the NW-GGap,
 377 where recent onshore and offshore observations show that slow earthquake indeed happen in a particular way, and thus where
 378 the mechanical properties of the plate interface are different (Cruz-Atienza et al., 2020; Plata-Martnez et al., 2020). Models B
 379 and C are remarkably different between stations ZIHP and CAYA, where the InSAR data used for model B does not play any

380 significant role. West of this region, model B predicts a very large shallow penetration of the SSE across the mechanically stable
381 zone where M7+ earthquakes occur every ~ 35 years (see past rupture areas)(UNAM, 2015). For this reason, model C, which
382 is consistent with our model A, is the most plausible solution for that zone. Besides, our resolution close to the ZIHP station
383 is higher than 60% as well. In conclusion, our preferred ELADIN solution has the most reliable features of both previously
384 published slip models.

385 **Conclusions**

386 We have introduced the ELADIN method, a new fault-slip inversion technique based on the adjoint elastostatic equations
387 under a constrained optimization framework. The method takes advantage of both the von Karman autocorrelation function
388 to control the problem of regularization and the gradient projection method to impose physically-consistent slip restrictions
389 (i.e. interplate coupling smaller than any given value and rake angles consistent with the relative plate motion). To account for
390 the data uncertainty, the method weights the observations according to their individual covariance using the precision matrix.
391 Synthetic slip inversions from strongly perturbed data show that the model restitution across the plate interface is surprisingly
392 high when this uncertainty is taken into account (i.e. for both SSE and coupled interface regions). The ELADIN method thus
393 allows determining the aseismic slip on any 3D plate interface (or any fault surface) by simultaneously inverting slipping and
394 coupled fault areas with a spectral control of the problem solution that guaranties a given resolution criterion. We defined
395 this criterion by means of the mobile checkerboard restitution index (*mcri*), which allows determining fault regions where the
396 resolution (i.e. the slip restitution index) is high enough for a given von Karman autocorrelation length, L . This means that the
397 inverted slip in those regions is valid (to some desired extent) within the wavenumber bandwidth associated to the von Karman
398 spectrum for that L .

399 After a thorough resolution analysis of the study region, we inverted the 2006 Guerrero SSE. Our preferred slip model (Model
400 A), obtained for $L = 30\text{km}$, was compared with two previously published solutions and found that it retains the most reliable
401 features of these two models. On one hand, our model is consistent with the solution of Cavalíé et al. (2013) (Model B) in that
402 it places the maximum slip region above 40 km depth (i.e. downdip from stations CAYA and COYU), where this solution is
403 well constrained by the InSAR data. On the other, although all solutions predict the SSE shallow penetration along a large part
404 of the NW-GGgap segment (west of CAYA), our resolution analysis clearly shows that this penetration might not be a reliable
405 feature of the 2006 SSE. However, our Model A is much closer to the solution of Radiguet et al. (2011) (Model C) close to
406 station ZIHP, where only GPS data is available. In this sense and considering also that M7+ earthquakes occur every ~ 35 years
407 east from that station (see previous rupture areas in Figure 10), which implies that the plate interface there is mechanically
408 unstable, then the extremely large updip SSE penetration predicted by Model B (Cavalíé et al., 2013) between stations ZIHP
409 and CAYA seems unrealistic.

410 A systematic application of the ELADIN method has been made in an associated work (Cruz-Atienza et al., 2020) to invert
411 recent data from the large GPS array shown in Figure 1, which has produced interesting results for the period 2016-2019, where
412 three major earthquakes and multiple SSEs occurred throughout the Mexican subduction zone.

413 **Acknowledgements**

414 We thank Mathilde Radiguet for providing the 2006 SSE data. The Somigliana tensor was computed in Miztli, UNAM cluster,
415 thanks to the CPU-hours assigned through the grant LANCAD-UNAM-DGTIC-312. SSE inversions were performed in the
416 Gaia supercomputing platform of the Institute of Geophysics at UNAM. This work was supported by UNAM-PAPIIT grants
417 IN113814 and IG100617, JICA-JST SATREPS-UNAM grant 15543611 and CONACyT grants 255308 and 6471.

418 **References**

- 419 Amey, R. M. J., Hooper, A., and Walters, R. J. (2018). A bayesian method for incorporating self-similarity into earthquake slip
420 inversions. *Journal of Geophysical Research: Solid Earth*, 123(7):6052–6071.
- 421 Askan, A., Akcelik, V., Bielak, J., and Ghattas, O. (2007). Full Waveform Inversion for Seismic Velocity and Anelastic Losses
422 in Heterogeneous Structures. *Bulletin of the Seismological Society of America*, 97(6):1990–2008.
- 423 Asnaashari, A., Brossier, R., Garambois, S., Audebert, F., Thore, P., and Virieux, J. (2013). Regularized seismic full waveform
424 inversion with prior model information. *Geophysics*, 78(2):R25–R36.
- 425 Bekaert, D. P. S., Hooper, A., and Wright, T. J. (2015). Reassessing the 2006 guerrero slow-slip event, mexico: Implications
426 for large earthquakes in the guerrero gap. *Journal of Geophysical Research: Solid Earth*, 120(2):1357–1375.
- 427 Calvetti, D., Morigi, S., Reichel, L., and Sgallari, F. (2000). Tikhonov regularization and the l-curve for large discrete ill-posed
428 problems. *Journal of computational and applied mathematics*, 123(1-2):423–446.
- 429 Campillo, M., Singh, S., Shapiro, N., Pacheco, J., and Herrmann, R. (1996). Crustal structure south of the mexican volcanic
430 belt, based on group velocity dispersion. *Geofisica Internacional*, 35(4):361–370.
- 431 Cavalié, O., Pathier, E., Radiguet, M., Vergnolle, M., Cotte, N., Walpersdorf, A., Kostoglodov, V., and Cotton, F. (2013). Slow
432 slip event in the mexican subduction zone: Evidence of shallower slip in the guerrero seismic gap for the 2006 event revealed
433 by the joint inversion of insar and gps data. *Earth and Planetary Science Letters*, 367:5260.
- 434 Coutant, O. (1990). Programme de simulation numérique AXITRA. *Rapport LGIT*, Université Joseph Fourier, Grenoble,
435 France.

- 436 Cruz-Atienza, V., Tago, J., Villafuerte, C., Wei, R., Garza-Girn, R., Domnguez, L., Kostoglodov, V., Nishimura, T., Franco, S.,
437 Real, J., Santoyo, M., Ito, Y., and Kazachkina, E. (2020). Short-term interaction between silent and devastating earthquakes
438 in mexico. Submitted to Science.
- 439 CruzAtienza, V. M., Ito, Y., Kostoglodov, V., Hjrleifsdttir, V., Iglesias, A., Tago, J., Cal, M., Real, J., Husker, A., Ide, S.,
440 Nishimura, T., Shinohara, M., MorteraGutierrez, C., Garca, S., and Kido, M. (2018). A Seismogeodetic Amphibious Network
441 in the Guerrero Seismic Gap, Mexico. Seismological Research Letters, 89(4):1435–1449.
- 442 Dragert, H., Wang, K., and James, T. S. (2001). A silent slip event on the deeper cascadia subduction interface. Science,
443 292(5521):1525–1528.
- 444 Fichtner, A., Bunge, H.-p., and Igel, H. (2006). The adjoint method in seismology: I. theory. Physics of the Earth and Planetary
445 Interiors, 157:86–104.
- 446 Fichtner, A., Kennett, B., Igel, H., and Bunge, H.-p. (2010). Full waveform tomography for radially anisotropic structure: New
447 insights into present and past states of the australasian upper mantle. Earth and Planetary Science Letters, 290:270–280.
- 448 Fukuda, J. and Johnson, K. M. (2008). A fully bayesian inversion for spatial distribution of fault slip with objective smoothing.
449 Bulletin of the Seismological Society of America, 98(3):1128–1146.
- 450 Gauthier, O., Virieux, J., and Tarantola, A. (1986). Two-dimensional nonlinear inversion of seismic waveforms: Numerical
451 results. Geophysics, 51(7):1341–1519.
- 452 Kostoglodov, V., Husker, A., Shapiro, N. M., Payero, J. S., Campillo, M., Cotte, N., and Clayton, R. (2010). The 2006 slow
453 slip event and nonvolcanic tremor in the mexican subduction zone. Geophysical Research Letters, 37(24).
- 454 Kostoglodov, V., Singh, S. K., Santiago, J. A., Franco, S. I., Larson, K. M., Lowry, A. R., and Bilham, R. (2003). A large silent
455 earthquake in the guerrero seismic gap, mexico. Geophysical Research Letters, 30(15).
- 456 Krischer, L., Fichtner, A., Boehm, C., and Igel, H. (2018). Automated large-scale full seismic waveform inversion for north
457 america and the north atlantic. Journal of Geophysical Research: Solid Earth, 123(7):5902–5928.
- 458 Mai, P. M. and Beroza, G. C. (2002). A spatial random field model to characterize complexity in earthquake slip. Journal of
459 Geophysical Research: Solid Earth, 107(B11):ESE 10–1–ESE 10–21.
- 460 McCaffrey, R., Qamar, A., King, R., Wells, R., Khazaradze, G., Williams, C., Stevens, C., Vollick, J., and Zwick, P. (2007).
461 Fault locking, block rotation and crustal deformation in the pacific northwest. Geophysical Journal International - GEOPHYS
462 J INT, 169:1315–1340.
- 463 Métivier, L. and Brossier, R. (2016). The seiscopes optimization toolbox: A large-scale nonlinear optimization library based on
464 reverse communicationthe seiscopes optimization toolbox. Geophysics, 81(2):F1–F15.

- 465 Minson, S. E., Simons, M., and Beck, J. L. (2013). Bayesian inversion for finite fault earthquake source models I theory and
466 algorithm. Geophysical Journal International, 194(3):1701–1726.
- 467 Miyazaki, S., Segall, P., McGuire, J. J., Kato, T., and Hatanaka, Y. (2006). Spatial and temporal evolution of stress and slip rate
468 during the 2000 tokai slow earthquake. Journal of Geophysical Research: Solid Earth, 111(B3).
- 469 Nishimura, T., Hirasawa, T., Miyazaki, S., Sagiya, T., Tada, T., Miura, S., and Tanaka, K. (2004). Temporal change of
470 interplate coupling in northeastern japan during 19952002 estimated from continuous gps observations. Geophysical Journal
471 International, 157(2):901–916.
- 472 Nocedal, J. and Wright, S. J. (2006). Numerical Optimization. Springer, 2nd edition.
- 473 Nocquet, J. (2018). Stochastic static fault slip inversion from geodetic data with non-negativity and bound constraints.
474 Geophysical Journal International, 214(1):366–385.
- 475 Nocquet, J., Villegas-Lanza, J., Chlieh, M., Mothes, P., Rolandone, F., Jarrin, P., Cisneros, D., Alvarado, A., Audin, L.,
476 Bondoux, F., Martin, X., Font, Y., Rgnier, M., Valle, M., Tran, T., Beauval, C., Maguia-Mendoza, J., Martinez, W., Tavera,
477 H., and Yepes, H. (2014). Motion of continental slivers and creeping subduction in the northern Andes. Nature Geoscience,
478 214(7).
- 479 Ozawa, S., Nishimura, T., Suito, H., Kobayashi, T., Tobita, M., and Imakiire, T. (2011). Coseismic and postseismic slip of the
480 2011 magnitude-9 tohoku-oki earthquake. Nature, 475(7356):373–376.
- 481 Plata-Martnez, R., S., I., Shinohara, M., Garca, E., Mizuno, N., Domnguez, L., Taira, T., Yamashita, Y., Toh, A., Yamada, T.,
482 Real, J., Husker, A., Cruz-Atienza, V., and Ito, Y. (2020). Shallow slow earthquakes and subducted bathymetry to decipher
483 devastating earthquakes in the guerrero seismic gap. Submitted to Science.
- 484 Radiguet, M., Cotton, F., Vergnolle, M., Campillo, M., Valette, B., Kostoglodov, V., and Cotte, N. (2011). Spatial and temporal
485 evolution of a long term slow slip event: the 2006 Guerrero Slow Slip Event. Geophys. J. Int., 184:816–828.
- 486 Radiguet, M., Cotton, F., Vergnolle, M., Campillo, M., Walpersdorf, A., Cotte, N., and Kostoglodov, V. (2012). Slow slip events
487 and strain accumulation in the Guerrero gap, Mexico. J. Geophys. Res., 117.
- 488 Sánchez-Reyes, H. S., Tago, J., Métivier, L., Cruz-Atienza, V., and Virieux, J. (2018). An evolutive linear kinematic source
489 inversion. Journal of Geophysical Research: Solid Earth, 123(6):4859–4885.
- 490 Savage, J. C. (1983). A dislocation model of strain accumulation and release at a subduction zone. Journal of Geophysical
491 Research: Solid Earth, 88(B6):4984–4996.
- 492 Simpson, R., Schulz, S., Dietz, L., and Burford, s. R. (1988). The response of creeping parts of the san andreas fault to
493 earthquakes on nearby faults: Two examples. pure and applied geophysics, 126(2-4):665–685.

- 494 Somala, S. N., Ampuero, J.-P., and Lapusta, N. (2018). Finite-fault source inversion using adjoint methods in 3-d heterogeneous
495 media. Geophysical Journal International, 214(1):402–420.
- 496 Tarantola, A. (1984). Inversion of seismic reflection data in the acoustic approximation. Geophysics, 49(8):1259–1266.
- 497 Tarantola, A. and Valette, B. (1982). Generalized nonlinear inverse problems solved using the least squares criterion. Reviews
498 of Geophysics, 20(2):219–232.
- 499 Tromp, J., Tape, C., and Liu, Q. (2005). Seismic tomography, adjoint methods, time reversal and banana-doughnut kernels.
500 Geophysical Journal International, 160(1):195–216.
- 501 UNAM, S. (2015). Papanao, mexico earthquake of 18 april 2014 (mw7.3). Geofisica Internacional, 54:363–386.
- 502 Vergnolle, M., Walpersdorf, A., Kostoglodov, V., Tregoning, P., Santiago, J., Cotte, N., and Franco, S. (2010). Slow slip events
503 in mexico revised from the processing of 11 year gps observations. Journal of Geophysical Research: Solid Earth, 115(B8).
- 504 Villafuerte, C. and Cruz-Atienza, V. M. (2017). Insights into the causal relationship between slow slip and tectonic tremor in
505 guerrero, mexico. Journal of Geophysical Research: Solid Earth, 122(8):6642–6656.
- 506 Wallace, L. M. and Beavan, J. (2010). Diverse slow slip behavior at the hikurangi subduction margin, new zealand. Journal of
507 Geophysical Research: Solid Earth, 115(B12).
- 508 Yabuki, T. and Matsu'Ura, M. (1992). Geodetic data inversion using a bayesian information criterion for spatial distribution of
509 fault slip. Geophysical Journal International, 109(2):363–375.

510 **A Gradient projection method: Cauchy point calculation**

511 The Cauchy point is an optimal state computed with a descent direction that respects the feasible solution region. We begin by
512 reformulating our inverse problem, eqs. (9-11), as the quadratic problem

$$\frac{1}{2} \underline{D}^T \underline{G} \underline{D} + \underline{c}^T \underline{D}, \quad (16)$$

513 subject to

$$D_i^{j,l} \leq (\underline{E} \underline{D})_i \leq D_i^{j,u}, \quad i \in \{p, c\} \wedge j \in \{\text{SSE, Coupling}\} \text{ regime}, \quad (17)$$

514 where

$$\underline{G} = \underline{F}^T \underline{T}^T \underline{C}_d^{-1} \underline{T} \underline{F} + \beta \underline{F}^T \underline{W}^T \underline{W} \underline{F}, \quad (18)$$

$$\underline{c} = - \left[\underline{U}_o^T \underline{C}_d^{-1} \underline{T} \underline{F} + \underline{D}_p^T \underline{W}^T \underline{W} \underline{F} \right]. \quad (19)$$

515 The gradient without considering the inequality constraint, eq. (17), is

$$\underline{g} = \underline{G} \underline{D} + \underline{c}, \quad (20)$$

516 First, we need to identify the step lengths for which each slip component reaches its bound along the direction $-\underline{g}$ and store
517 them in \bar{t} . Then, we eliminate duplicate and zero values of \bar{t} to obtain a sorted reduced set of breakpoints $\{t_1, t_2, \dots, t_l\}$ such
518 that $t_i < t_{i+1}$ for $i \in \{1, 2, \dots, l-1\}$. With this set, we construct a set of intervals like $\{[0, t_1], [t_1, t_2], \dots, [t_{l-1}, t_l]\}$. Suppose
519 that we have not found the minimizer up to the interval $[t_{j-1}, t_j]$, then we can model the slip along that interval as

$$\underline{D}(t) = \underline{D}(t_{j-1}) + (\Delta t) \underline{p}^{j-1}, \quad (21)$$

520 where

$$\Delta t = t - t_{j-1} \in [0, t_j - t_{j-1}], \quad (22)$$

$$\underline{p}_i^{j-1} = \begin{cases} -g_i & \text{if } t_{j-1} < \bar{t}_i, \\ 0 & \text{otherwise.} \end{cases} \quad (23)$$

521 If we substitute eq. (21) in the quadratic cost function (16), we leave it as a function of Δt

$$q(\Delta t) = \frac{1}{2} (\underline{D}(t_{j-1}) + (\Delta t) \underline{p}^{j-1})^T \underline{G} (\underline{D}(t_{j-1}) + (\Delta t) \underline{p}^{j-1}) + \underline{c}^T (\Delta t) \underline{p}^{j-1}, \quad (24)$$

522 which can be reformulated as

$$q(\Delta t) = f_{j-1} + g_{j-1}\Delta t + \frac{1}{2}h_{j-1}(\Delta t)^2, \quad (25)$$

523 where

$$f_{j-1} = \frac{1}{2}D(t_{j-1})^T \underline{\mathbf{G}} D(t_{j-1}) + \underline{\mathbf{c}}^T \underline{\mathbf{D}}(t_j - 1), \quad (26)$$

$$g_{j-1} = D(t_{j-1})^T \underline{\mathbf{G}} \underline{\mathbf{p}}^{j-1} + \underline{\mathbf{c}}^T \underline{\mathbf{p}}^{j-1}, \quad (27)$$

$$h_{j-1} = (\underline{\mathbf{p}}^{j-1})^T \underline{\mathbf{G}} \underline{\mathbf{p}}^{j-1}. \quad (28)$$

524 The solution of this problem is

$$\Delta t^* = -\frac{g_{j-1}}{h_{j-1}}. \quad (29)$$

525 Only one of the following three cases can occur

- 526 (i) If $g_{j-1} > 0$ the minimizer is at $\Delta t^* = 0$ with $t^* = t_{j-1}$ and $p^* = p_{j-1}$.
- 527 (ii) If $\Delta t^* \in [0, t_j - t_{j-1})$ the minimizer is in the interval with $t^* = t_{j-1}$ and $p^* = p_{j-1}$.
- 528 (iii) If $\Delta t^* > t_j - t_{j-1}$ then try the nex interval.

529 Once the optimal step has been found, Δt^* , the Cauchy point is evaluated as

$$\underline{\mathbf{D}}^c = \underline{\mathbf{D}}(t^*) + \Delta t^* \underline{\mathbf{p}}^*. \quad (30)$$

530 B Gaussian slip inversions

531 Figures S1 and S2 show the synthetic data inversions and restitution indexes with and without noise of the Gaussian-like pulses
532 shown in Figures 4A and 4B, respectively.

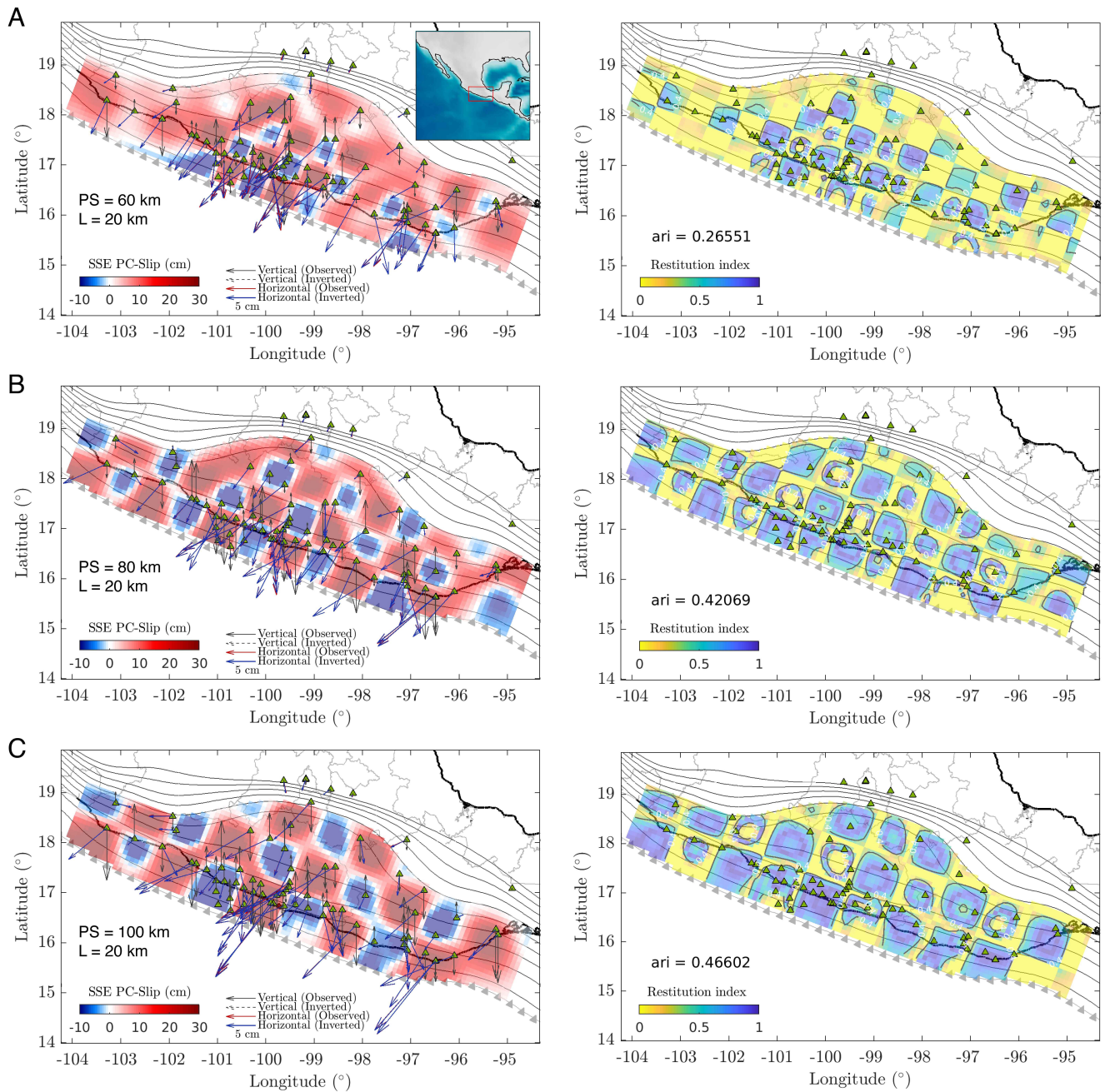


Figure 1: Checkerboard inversions for PS of (A) 60, (B) 80 and (C) 100 km, and correlation length, L , of 20 km. The inverted slip along with the surface displacement fits (left column) and the associated restitution index (right column) are displayed on the 3D plate interface (gray contours). Green triangles are the GPS stations.

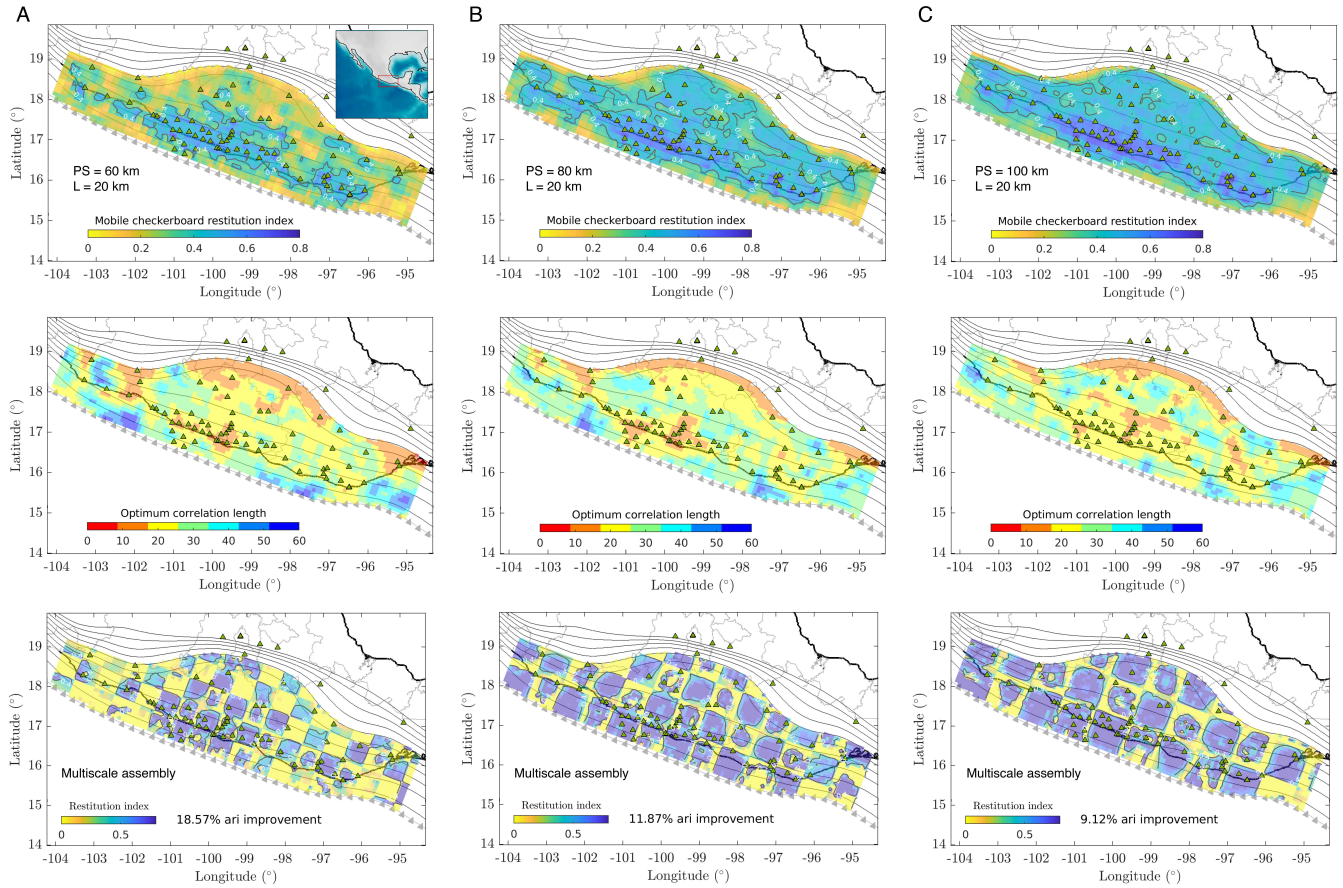


Figure 2: MOC tests for PS of (A) 60, (B) 80 and (C) 100 km and correlation length, L , of 20 km. Distributions of $mcri$ (first row), the optimum correlation length (second row) and the multiscale assembly of the restitution index (i.e. computed from the assembly of the best slip solutions for the CBs shown in Figure 1), all of them displayed on the 3D plate interface (gray contours). Green triangles are the GPS stations.

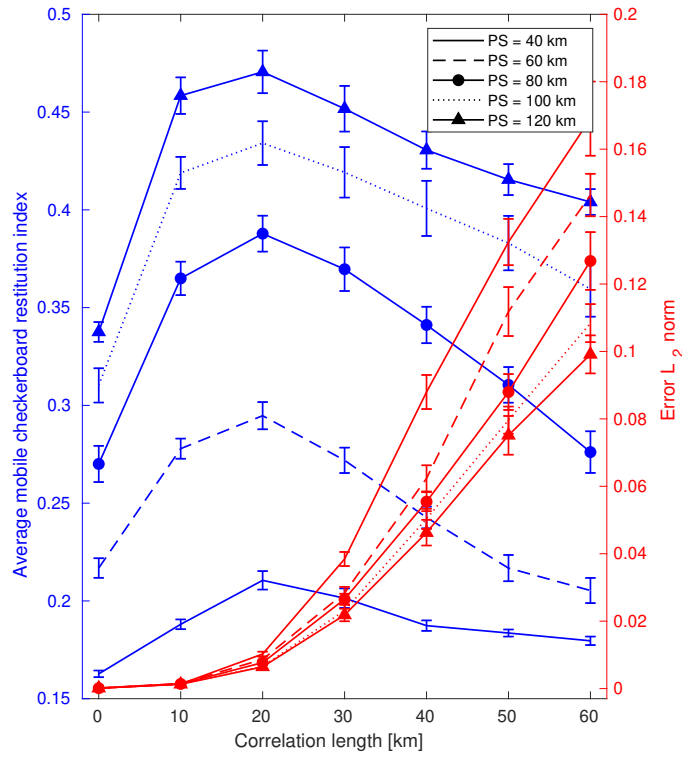


Figure 3: Results from all MOC tests in terms of the whole-interface average *meri* (blue) and the average data-misfit error (red) as a function of the inversions correlation length L . PS (Patch Size) refers to the slip-patch characteristic length (i.e. the checkerboard unit size).

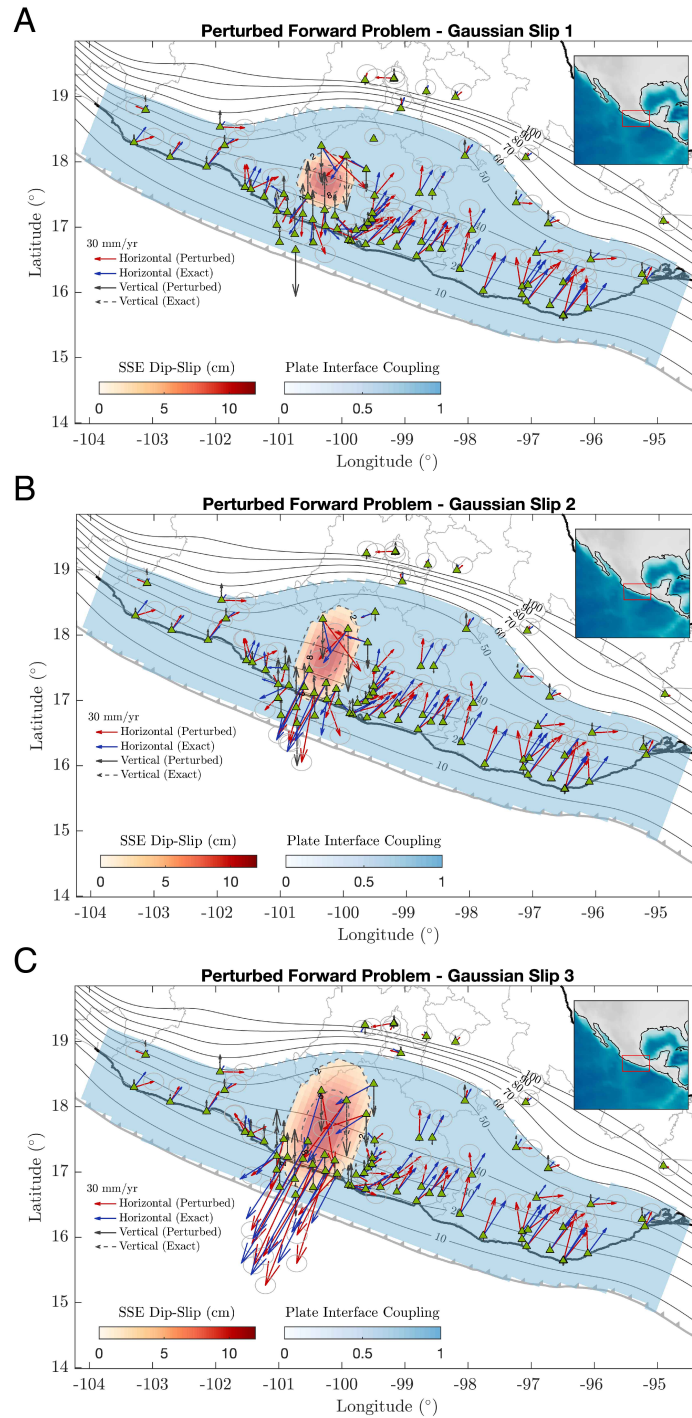


Figure 4: Slip models on the plate interface (background colors) and the associated model displacement predictions (arrows) for three Gaussian-like slip patches with different characteristic lengths. Blue and black-solid arrows show the exact surface displacements while red and black-dashed arrows show the same predictions but stochastically perturbed according to the normal distributions given by the data variance per component.

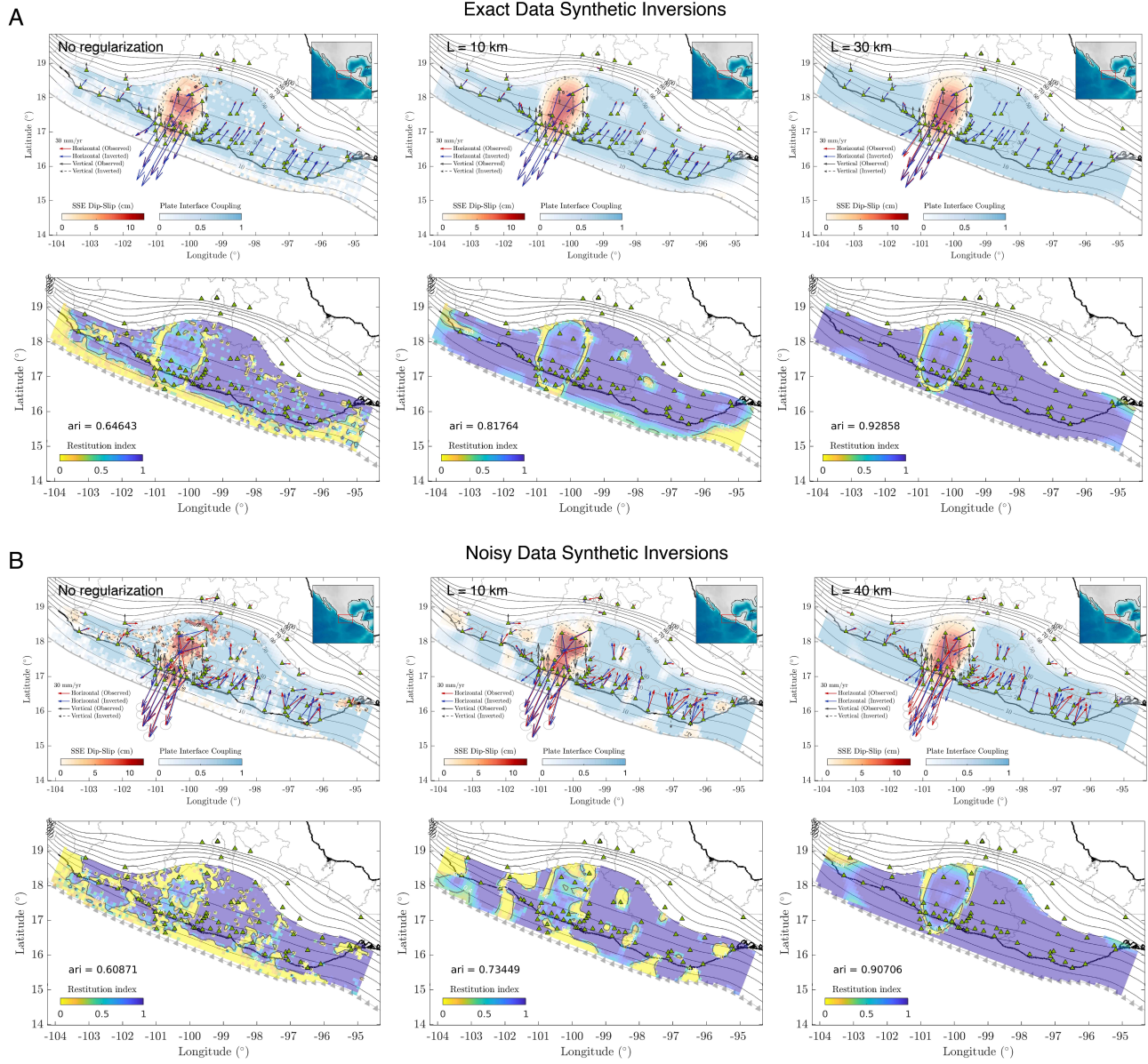


Figure 5: Synthetic inversion results for the slip model shown in Figure 4C from the exact target displacements (panel A) and from the perturbed (noisy) displacements (panel B). The second row of each panel shows the distribution of the restitution index over the plate interface without regularization and for different values of the correlation length, L.

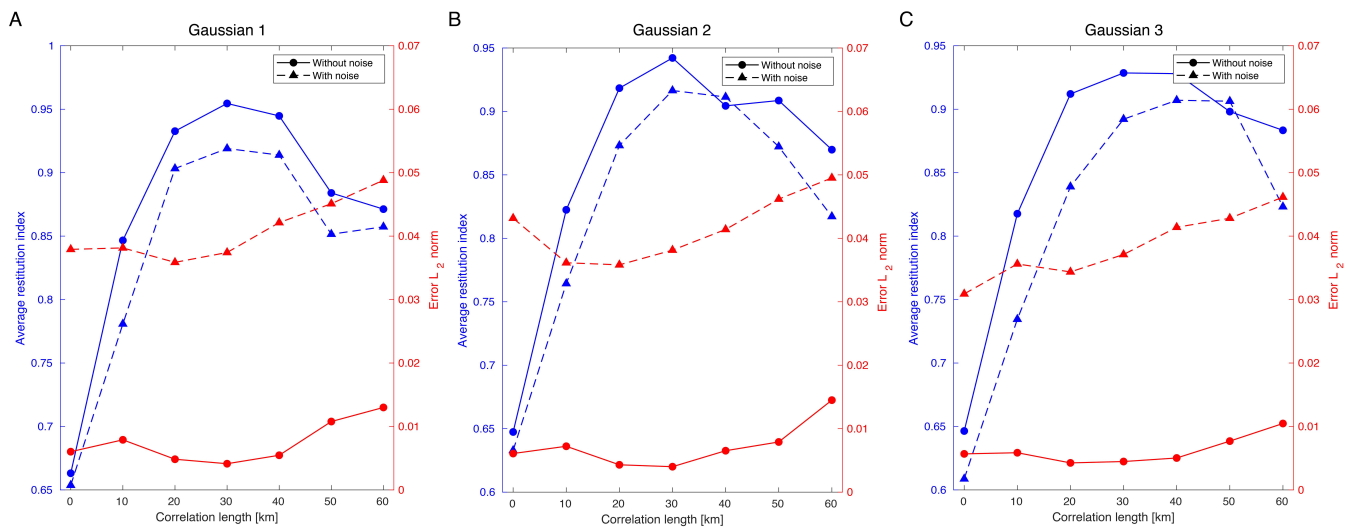


Figure 6: Synthetic inversion results for the three Gaussian-like slip functions shown in Figure 4 in terms of the whole-interface average restitution index (ari) and average data-misfit error (red) as a function of the inversions correlation length L . Solid lines correspond to the inversions using the exact data while dashed lines to the inversions with noisy data (see Figure 4). Notice that in all cases the maximum restitutions (ari) are above 0.9.

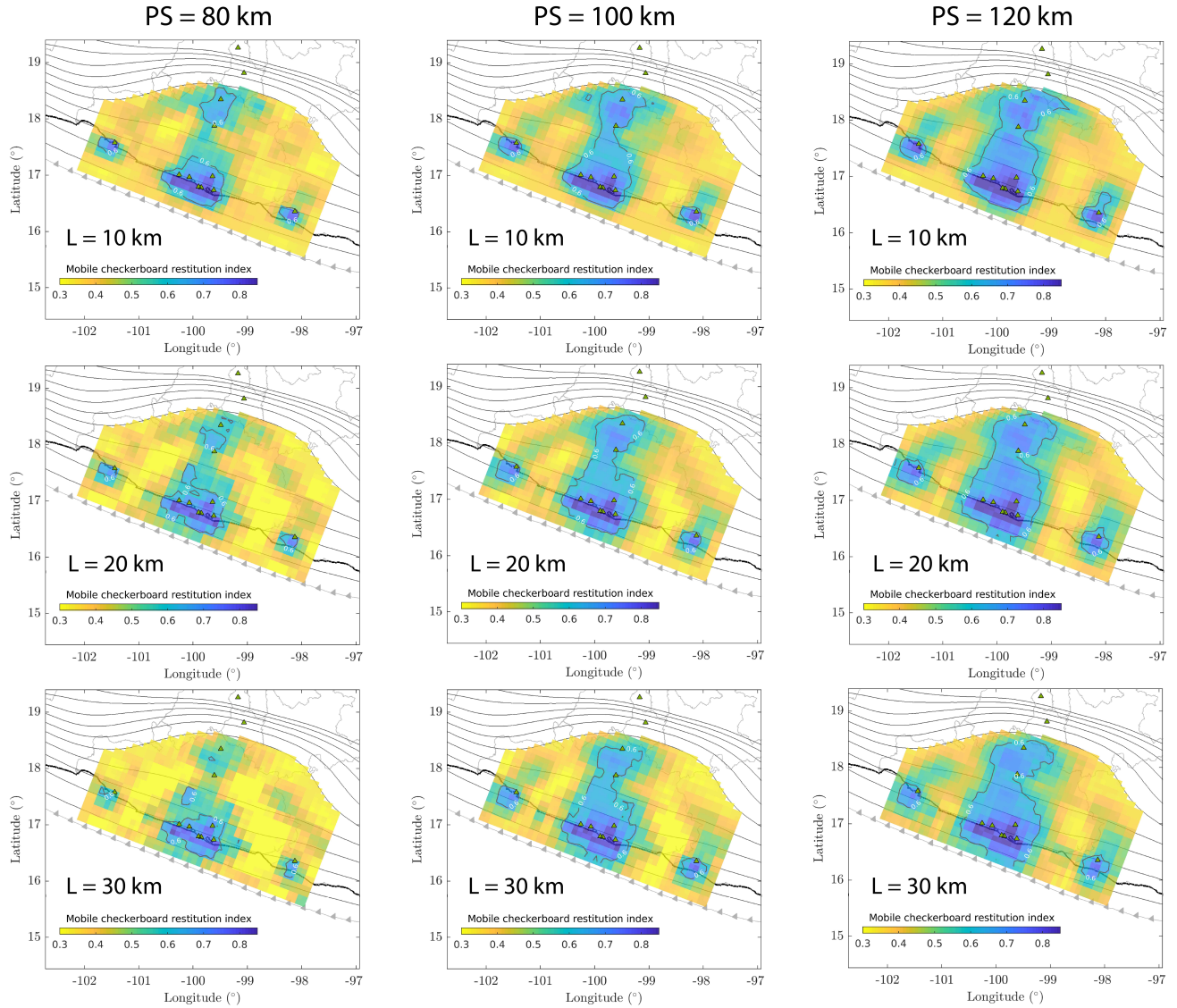


Figure 7: Plate interface distribution of the mobile checkerboard restitution index ($mcri$) for MOC tests corresponding to patch sizes (PS) of 80, 100 and 120 km and correlation lengths $L = 10, 20$ and 30 km for the 2006 SSE stations configuration. Black contours correspond to $mcri$ values of 0.6 (i.e. slip resolution of 60%).

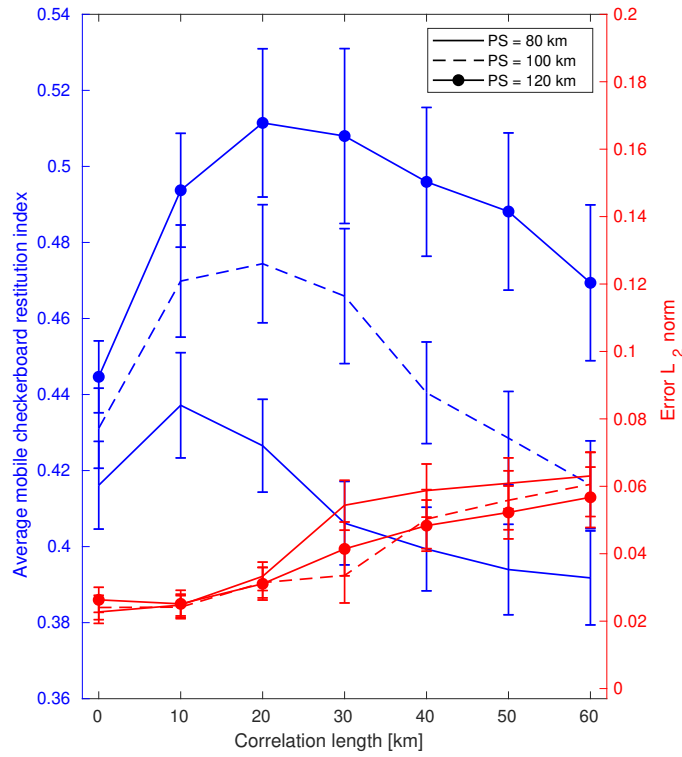


Figure 8: Results from all MOC tests for the 2006 SSE stations configuration in terms of the whole-interface average $mcri$ (blue) and the average data-misfit error (red) as a function of the inversions correlation length L . PS (Patch Size) refers to the slip-patch characteristic length (i.e. the checkerboard unit size).

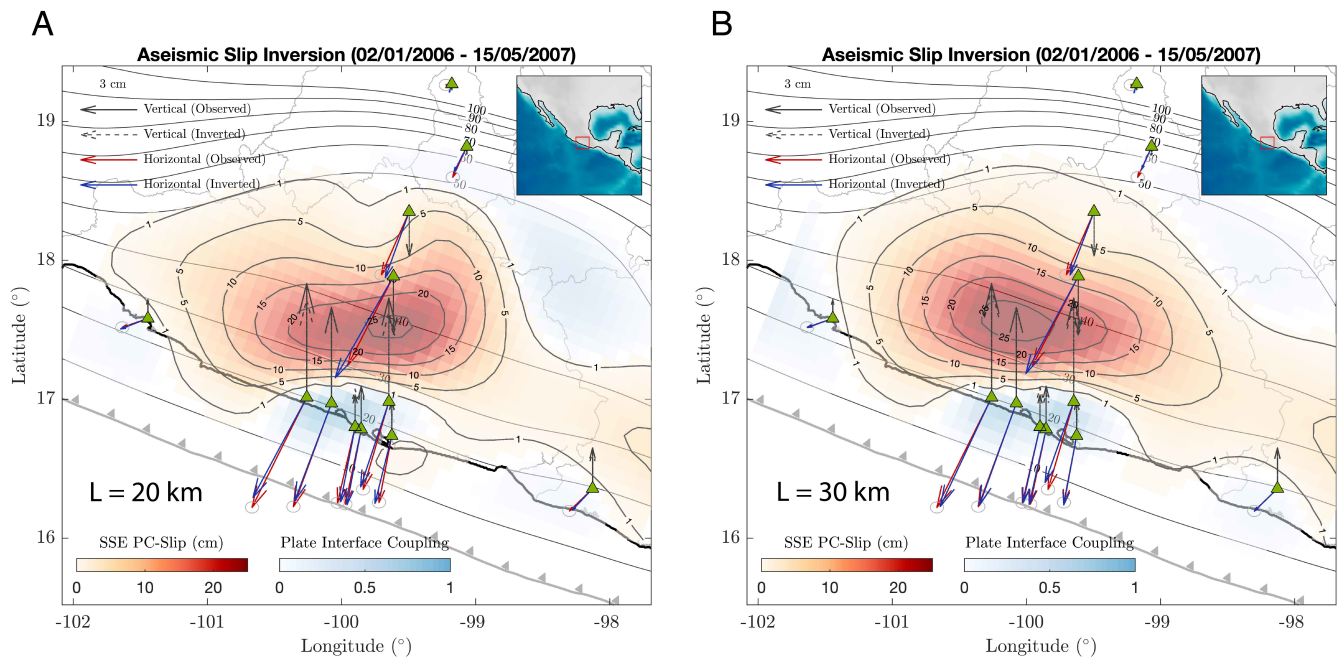


Figure 9: Aseismic slip inversions (in the plate convergence (PC) direction) of the 2006 Guerrero SSE for correlation lengths $L = 20$ km (A) and $L = 30$ km (B). The plate interface coupling is determined from the ratio between the back slip and the cumulative slip in the inverted period given a plate convergence rate of 6 cm/yr.

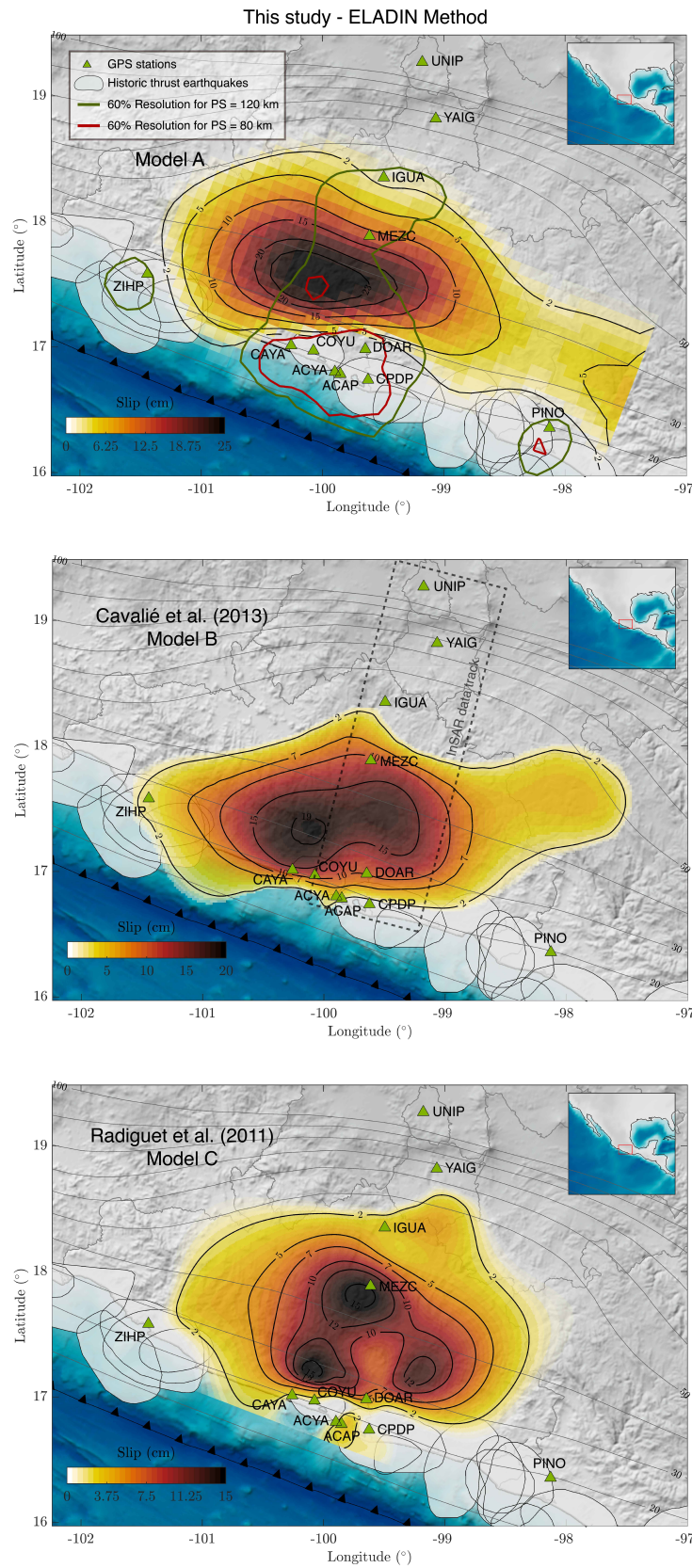


Figure 10: Comparison of our preferred solution (model A - for $L = 30$ km, Figure 9) with two previously published model for the 2006 Guerrero SSE, the one of Cavalié et al. (2013) (model B) and the one of Radiguet et al. (2011) (model C). 60% resolution contours for slip-patch (PS) characteristic lengths of 80 and 120 km are shown over model A.

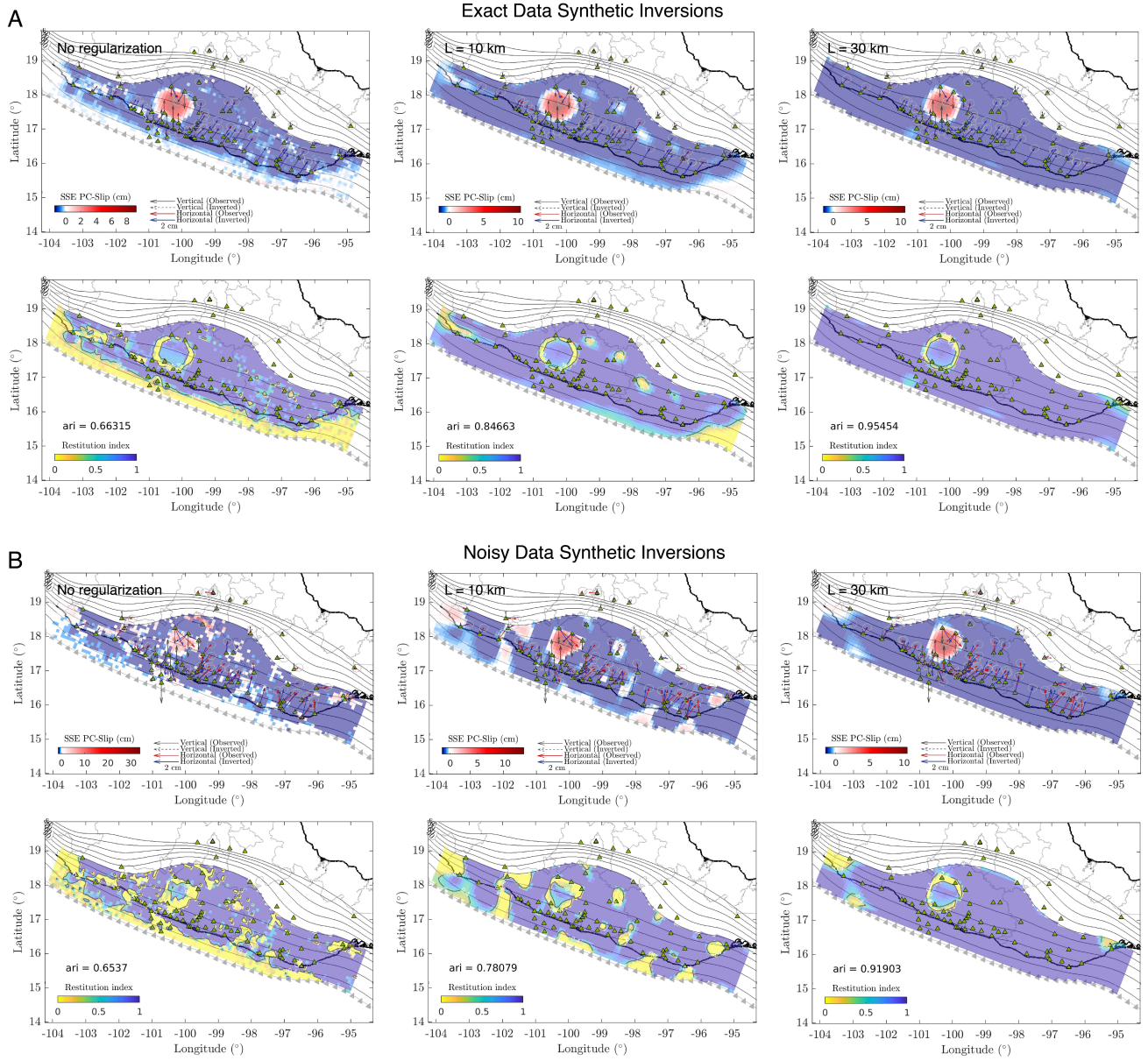


Figure S1: Synthetic inversion results for the Gaussian-like slip model shown in Figure 4A from the exact target displacements (panel A) and from the perturbed (noisy) displacements (panel B). The second row of each panel shows the distribution of the restitution index over the plate interface without regularization and for different values of the correlation length, L .

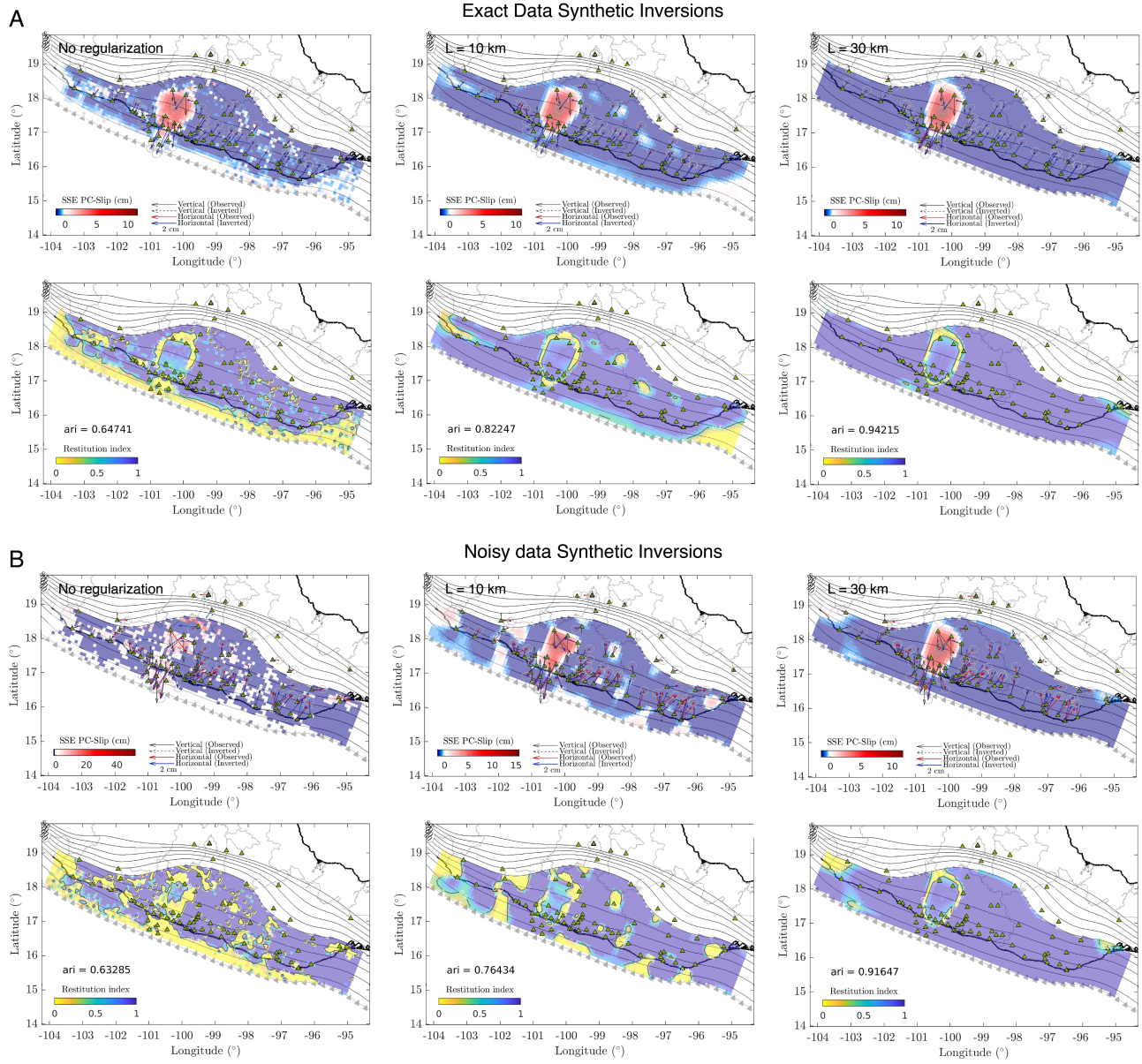


Figure S2: Synthetic inversion results for the Gaussian-like slip model shown in Figure 4B from the exact target displacements (panel A) and from the perturbed (noisy) displacements (panel B). The second row of each panel shows the distribution of the restitution index over the plate interface without regularization and for different values of the correlation length, L .